Acta Neuropathologica (2024) 147:101
https://doi.org/10.1007/s00401-024-02751-9

ORIGINAL PAPER

Brain vasculature accumulates tau and is spatially related to tau tangle pathology in Alzheimer's disease

Zachary Hoglund[1] · Nancy Ruiz-Uribe[1,2] · Eric del Sastre[1] · Benjamin Woost[1] · Elizabeth Bader[1] · Joshua Bailey[1] · Bradley T. Hyman[1,2] · Theodore Zwang[1,2] · Rachel E. Bennett[1,2]

Received: 2 April 2024 / Revised: 5 June 2024 / Accepted: 5 June 2024

Abstract

Insoluble pathogenic proteins accumulate along blood vessels in conditions of cerebral amyloid angiopathy (CAA), exerting a toxic effect on vascular cells and impacting cerebral homeostasis. In this work, we provide new evidence from three-dimensional human brain histology that tau protein, the main component of neurofibrillary tangles, can similarly accumulate along brain vascular segments. We quantitatively assessed n = 6 Alzheimer's disease (AD), and n = 6 normal aging control brains and saw that tau-positive blood vessel segments were present in all AD cases. Tau-positive vessels are enriched for tau at levels higher than the surrounding tissue and appear to affect arterioles across cortical layers (I–V). Further, vessels isolated from these AD tissues were enriched for N-terminal tau and tau phosphorylated at T181 and T217. Importantly, tau-positive vessels are associated with local areas of increased tau neurofibrillary tangles. This suggests that accumulation of tau around blood vessels may reflect a local clearance failure. In sum, these data indicate that tau, like amyloid beta, accumulates along blood vessels and may exert a significant influence on vasculature in the setting of AD.

Keywords Alzheimer's disease · Tau · Neurofibrillary tangles · Blood vessels · Cerebral vasculature · Cerebral amyloid angiopathy

Introduction

The formation of tau-containing neurofibrillary tangles (NFTs) is closely associated with the severity and progression of Alzheimer's disease (AD) [2, 8]. Because of this close relationship, it is important to investigate the mechanisms by which these pathological aggregates of tau protein form, and why certain neurons are more vulnerable to tangle formation than others. On the molecular scale, NFTs form when tau protein is post-translationally modified, notably by phosphorylation at multiple sites in the protein's structure, increasing its propensity to self-aggregate. In AD, aggregates develop in distinct regional patterns, including with varying density between cortical layers [1, 26]. These observations indicate that neuroarchitecture plays a significant role in the progression of tau pathology. In addition to intracellular accumulation in neurons, tau is also secreted into the extracellular space and can be detected in cerebrospinal fluid and blood [4, 17, 32, 44].

Given that that tau is present extracellularly, we hypothesized that one key mechanism that may influence the local accumulation of tau pathology could be vascular brain clearance pathways [36]. Peri- and para-vascular clearance pathways serve as important routes for the removal of brain solutes, linking the interstitial (ISF) and cerebrospinal fluid (CSF) compartments, while trans-vascular clearance may directly transport other molecules from the brain to the blood. Reduced export of protein wastes along these pathways is believed to lead to the accumulation of toxic and aggregation-prone species of AD-related proteins [18, 20, 21, 38]. This is most clearly exemplified by cerebral amyloid angiopathy (CAA), a common AD co-pathology in which insoluble amyloid beta accumulates in the basement

Theodore Zwang and Rachel E. Bennett have contributed equally to this work.

✉ Theodore Zwang
tzwang@mgh.harvard.edu

✉ Rachel E. Bennett
rebennett@mgh.harvard.edu

[1] Department of Neurology, Massachusetts General Hospital, 114 16Th Street, Charlestown, MA, USA

[2] Harvard Medical School, Boston, MA, USA

membrane and smooth muscle cells of leptomeningeal and penetrating arterioles in the brain. In a recent study, Harrison et al. showed that globally perturbing the CSF-ISF flow accelerated tau deposition in the brains of a mouse model [18]. This work demonstrated that this system is important not just for amyloid beta but also for tau protein clearance; however, it did not examine individual vessels to understand their direct contribution to pathology. In related work, our group observed that isolated vasculature from both tauopathy mice and human AD brains contains high levels of bioactive tau capable of seeding new aggregates [5]. Together, this suggests that impaired clearance of these bioactive tau species could result in vasculature becoming important reservoirs for tau protein.

In this study, we identified the presence of tau immunoreactivity along cerebral brain vessels in AD patients and sought to quantify the relationship between tau pathology and brain vasculature at smaller, single-cell spatial scales. We predicted that if impaired perivascular clearance is related to the formation of tau tangles, increased phosphorylated tau species would be present along blood vessels in the brain and tangles would exhibit close spatial relationships with vasculature compared to non-tangle bearing neurons. However, one challenge of investigating protein distribution in the brain is imaging structures at high resolution in large tissue volumes. Advances in tissue clearing and multiplexed antibody staining have addressed this gap and enabled us to quantify the distribution of tau pathology and determine its spatial relationship to vasculature in the AD brain with single-cell resolution [45, 46]. This allowed us to quantify, in three dimensions, the proximity of phosphorylated tau and NFTs to individually segmented blood vessels. In addition, we conducted protein assays to determine the presence of bioactive tau species in vasculature. Surprisingly, these experiments uncovered new evidence that, like CAA, tau accumulates along vascular segments in the AD brain. Additionally, NFT density positively correlated with the amount of tau accumulated along vascular segments, indicating that tau accumulation along vasculature is associated with tangle formation in Alzheimer's disease.

Materials and methods

Human tissues. Fresh frozen human tissue samples of the inferior temporal gyrus were provided by the Massachusetts Alzheimer's Disease Research Center (ADRC) with approval from the Mass General Brigham IRB (1999P009556) and with informed consent of patients or their relatives. In total, 7 human participants with AD and 9 controls were selected from the Massachusetts Alzheimer's Disease Research Center. For quantitative imaging experiments a sex-matched group (3F/3M) of donor tissues with and without AD pathology were selected for comparison. Additional samples were utilized for biochemistry and protocol optimization experiments. All samples were rigorously evaluated using standard histological methods by trained neuropathologists in the ADRC and detailed information for all donor tissues including sex, age at death, Thal stage, Braak stage, CERAD scores, post-mortem interval, *APOE* genotype, and comorbidities are listed in Table 1 [19].

Protocol for assaying tau extracted from blood vessel homogenates

Isolation of blood vessels. Blood vessels were isolated from 200 to 300 mg of frozen mice and human tissue. Brains were minced in 2 mm sections using a razor blade in ice-cold B1 buffer (Hanks Balanced Salt Solution with 10 mM HEPES, pH 7; Thermo Fisher Scientific). Then samples were manually homogenized using a Dounce homogenizer with 12 strokes. Homogenate was then transferred into a conical tube filled with 20 mL of B1 buffer and centrifuged at 2000*g* for 10 min at 4 ºC. Supernatant was discarded and the pellet was vigorously resuspended for 1 min in 20 mL of B2 buffer (B1 buffer with 18% dextran, Sigma-Aldrich) to remove myelin. Samples were centrifuged at 4400*g* for 15 min at 4 ºC. The myelin layer was carefully detached, and the pellet was resuspended in 1 mL of B3 buffer (B1 buffer with 1% Bovine Serum Albumin, BSA, Sigma-Aldrich). Afterward, homogenate was filtered through a 20 µm mesh (Millipore) previously equilibrated with 5 mL of ice-cold B3 solution. Brain blood vessels were rinsed with 30 mL of ice-cold B3 solution and then the blood vessels were detached from the filters by immersing them in 30 mL of B3 ice-cold solution. Vessels were centrifuged at 2000*g* for 5 min at 4 ºC. Finally, the pellet was resuspended in 1 mL of ice-cold B1 solution and again centrifuged at 2000*g* for 5 min at 4 ºC and the supernatant was discarded. Vessel-containing pellets were stored at − 80 ºC.

Protein assays. Protein was extracted from human and mice brain blood vessel homogenates, which were sonicated at 20% amplitude in 10 pulses in PBS supplemented with protease and phosphatase inhibitors (cOmplete Mini and PhosSTOP EASYpack; Roche). Then, samples were centrifuged at 3000*g* for 5 min at 4 ºC and the supernatant was discarded. Proteins were analyzed using a capillary-based electrophoresis instrument (SimpleWes, Biotechne). Three mg of protein were used per sample. Protein separation and detection were performed by capillary electrophoresis, and the binding of antibodies and HRP conjugated secondaries was done in the SimpleWes machine. Antibodies used were phospho-T181 (mouse 1:50, MN10050, Invitrogen), phospho-S202 (rabbit 1:25, 39357S, Cell Signaling), phospho-T217 (rabbit 1:25, 44–744, Invitrogen), phospho-T231 (rabbit 1:50, #44–746, Invitrogen), Tau13 (mouse 1:50, 835,201,

Table 1 Human tissues used in this study

Sample number	Sex	Age at death	Thal stage	Braak stage	CERAD score	*APOE*	PMI (hrs)	Comorbidities
AD 1	M	74	5	V	3	4/4	10	CVD, CAA (3/4)
AD 2	M	75	5	VI	3	3/3	4	CVD
AD 3	M	≥90	4	III	2	3/4	14	CVD, CAA (2/4)
AD 4	F	66	5	VI	3	3/3	14	CVD
AD 5	F	≥90	5	VI	3	NA	5	Arteriolosclerosis, CAA (2/4)
AD 6	F	70	5	VI	3	3/4	24	CVD
fAD 7	M	52	5	V	3	NA	28	LBD, CAA (2/4), CVD
Ctrl 1	F	68	0	I	0	NA	20	CVD
Ctrl 2	M	62	1	0	0	NA	17	CVD
Ctrl 3	M	73	2	0	1	NA	14	CVD
Ctrl 4	M	63	2	0	0	NA	18	CVD
Ctrl 5	F	64	0	I	0	NA	18	CVD
Ctrl 6	F	56	1	0	0	NA	8	Acute Hypoxia
Ctrl 7	M	≥90	0	I	1	NA	24	CVD
Ctrl 8	F	73	0	0	0	NA	20	Infarcts, CVD
Ctrl 9	F	≥90	1	II	1	NA	8	CAA (1/4)

Details include sex (*M* male; *F* female), age at death (ages ≥ 90 have been aggregated according to HIPAA Privacy Rule de-identification standards), Braak stage, comorbidities (*CVD* cerebrovascular disease, *LBD* lewy body dementia, *CAA* cerebral amyloid angiopathy), and post-mortem interval (PMI; hours). For tissues with CAA, Vonsattel scores [42] are indicated in parentheses. In tissues with CVD, neuropathological lesions included mild to moderate atherosclerosis in the Circle of Willis, and mild to moderate arteriosclerosis in the leptomeninges and subcortical white matter. None of the inferior temporal gyrus areas examined contained overt vascular lesions. AD and Ctrl (Control) donors 1–6 were used for quantitative 3D imaging assessments. Sample AD 7 (familial AD, fAD; PSEN1 L435F mutation) was used for methods development, including optimizing antibody labeling protocols and was assessed qualitatively including for SMA labeling (Fig. 2F). Additional Ctrl samples 7–9 were used for biochemical assessments (Fig. 6) due to the availability of frozen tissue

Biolegend), Tau46 (mouse 1:50, 4019S, Cell Signaling) and total tau (rabbit 1:50, A0024, DAKO). Specific SimpleWes secondary antibodies HRP conjugated were acquired from the manufacturer (Biotechne). Protein quantification was analyzed in Fiji (https://doi.org/10.1038/nmeth.2019). The total intensity of signal in each lane was measured and normalized to the average of the three control samples.

Protocol for tissue clearing and imaging

Tissue slicing. Brain samples were placed in 4% paraformaldehyde (Thermo Fisher Scientific, cat No. 50980487) for 24 h at 4 °C. Tissue was then rinsed three times with 50 ml phosphate-buffered saline (PBS) for 10 min each, then placed in fresh PBS overnight at 4 °C and rinsed with fresh PBS. Fixed tissue underwent three rinsing cycles in 10-min increments using 50 ml of PBS, and then were placed in fresh PBS overnight at 4 °C. In preparation for tissue slicing, tissue was transferred to individual 35 mm Petri dishes and embedded in a gel block by pouring warm 4% agarose gel solution in PBS (4 g/100 ml) (Promega, cat No. V3121) over the tissue. The gel was then cooled to solidify and cut into a block to provide rigidity for cutting even slices. The tissue was secured on a vibratome (Leica Biosystems, VT1000 S Vibrating Blade Microtome) by super gluing the bottom of the agarose block. The vibratome was then used to slice 0.5–1 mm thick tissue sections. Each slice was then removed from the agarose through gentle manipulation with blunt forceps or paintbrushes and placed in a crosslinking solution, described below.

Delipidation. Tissue was then placed into sodium dodecyl sulfate (Sigma-Aldrich, cat No. L3771) 28.83 g/500 ml PBS-clearing solution supplemented with sodium borate (Sigma-Aldrich, cat No. S9640) on shaker at 100 rpm and 37 °C for ~3 days. After delipidation, the brain slices were rinsed with 50 ml PBS five times over 24 h.

Immunohistochemistry. Each brain slice was placed in a 2 ml Eppendorf tube that could hold the slice so its large, flat sides could be exposed to solution. PBST (PBS with 0.2% Triton X-100, Thermo Fisher Scientific) was added to just cover the top of the samples (~500 µl). Tissue was heated to 50 °C for 1 h in PBST and then cooled to room temperature prior to incubation with antibodies. Conjugated antibodies against the following epitopes were then added to the solution containing each tissue slice: phospho-tau Ser202, Thr205 (AT8, 1.6:500, Thermo Fisher, cat No. MN1020) conjugated to Alexa Fluor 647 (Thermo Fisher, cat No. A37573), HuD Antibody E-1 (1.6:500, Santa Cruz Biotechnology, cat No. sc-28299) conjugated to Alexa Fluor 555 (Thermo Fisher, cat No. A37571), Glut1 antibody

conjugated to Alexa Fluor 488 (EMD Millipore, 07-1401-AF488) and 4′,6-diamidino-2-phenylindole dihydrochloride (DAPI, 1.6:500, Sigma-Aldrich, cat No. 10236276001). An additional slice from each donor was separately incubated in an antibody mixture containing amyloid-beta conjugated to Alexa 488 (Cell Signaling Technology, cat No. 51374S), phospho-tau Ser 202, Thr205 conjugated to Alexa 555, and Glut1 conjugated to Alexa 647 antibodies. Tissue was incubated with primary antibodies for one week at 4 °C with gentle shaking. Following incubation, tissue was washed in fresh PBST 3 × 10 min and set on shaker for one week at 4 °C with gentle shaking.

Refractive index matching. After immunohistochemical staining, the samples were incubated with 80% glycerol and 20% deionized water for 24 h at room temperature with gentle shaking. Samples were then placed on a glass microscope slide with a 3D-printed ring that allowed the tissue to remain in a pool of glycerol during imaging. The ring was 3D-printed to match the thickness of the tissue (Formlabs) so a glass coverslip could be placed on top and seal the tissue in the glycerol.

Imaging. The tissue was imaged using Olympus Inverted Confocal FV3000 with a 10 × air objective, and multi-region images were stitched together using the microscope software (Fluoview FV31S-SW, Version 2.5.1.228). Additional higher resolution images were collected by placing the tissue in a bath of 80% glycerol in a Petri dish and imaged using a 20 × immersion objective (Zeiss Clr Plan-Neofluar 20x/1.0 Corr) with an inverted Zeiss 980 confocal microscope. Image Z-stacks were then reconstructed and visualized using Imaris microscopy image analysis software. Alternatively, a LifeCanvas Technologies megaSPIM light sheet microscope equipped with a 3.6 × lens was used, and refractive index matching was performed using EasyIndex (LifeCanvas Technologies).

Protocol for segmentation and quantification of pathology

Analysis with Ilastik (1.4.0). Imaging data for tau and HuD were converted to HDF5 format using Ilastik's ImageJ plugin [7]. The staining was then individually segmented for each image using Ilastik's pixel classifier workflow. In short, a paintbrush was used to draw over the signal and background to help train the classifier on how to segment each image. All images were then processed through the trained pixel classifier, and probability maps were exported as HDF5 formatted images. Pixel probability maps and raw data were loaded into Ilastik's object classification workflow and used to train object classifiers for each image. Tau object classifiers were trained by manually classifying objects as noise or tangles, and HuD object classifiers were trained by manually classifying objects as noise or neurons. Data were exported as object identities and spreadsheets with information about the objects' classification and characteristics, which were then loaded into MATLAB (r2023b) code to match objects from each channel with colocalized objects.

Separating objects into cortical layers. Imaris surface generation was used to draw regions around each cortical layer on individual imaging planes within the Z-stack, which was then merged into distinct volumes that contained each cortical layer. These volumes were then used to generate a new channel by masking the pixels contained within each volume and setting them equal to the cortical layer (i.e., pixels in layer 1 = 1, pixels in layer 2 = 2, etc.) and pixels not within a clearly defined layer equal to zero. This channel was then exported as a single multipage tiff stack, which could be loaded into our MATLAB code to identify the cortical layer for each object output by Ilastik.

Blood vessel segmentation. Individual blood vessels were manually segmented from clear brain images using a virtual reality image analysis software (Syglass). Segmentation was performed blinded to disease status, using the GLUT1 channel alone. Based on initial qualitative analysis, where tau accumulation along capillaries was not apparent, blood vessels with diameters of approximately 20 μm that spanned multiple cortical layers were selected for segmentation. Using these criteria resulted in the selection of 16–26 blood vessels, or roughly all traceable non-capillary vessels, were manually masked and segmented in each sample. Diameters were measured by drawing a line across the center cross section of each blood vessel and averaging three measures taken from separate locations. Individually masked blood vessels were then realigned with their original image in Imaris, and distance transforms were calculated and exported for each blood vessel.

Intensity and density calculation and binning (MATLAB r2023b). MATLAB scripts were developed to calculate the intensity of tau staining, neuron density, and tau tangle density, along and away from the segmented blood vessels' surfaces. First, tau data, segmented blood vessel distance transform images, and segmented cortical layer images were loaded simultaneously in one MATLAB script to align all images and export coordinates for data within 100 microns of the blood vessels' surfaces. These coordinates contained data for each pixel in this range, with their X, Y, and Z positions; tau intensity; and cortical layer. To account for staining differences in each sample, tau intensity was normalized between samples using a piecewise linear normalization. The pixel intensity for background, autofluorescence, and AT8 positivity were recorded in each sample at 3 depths in the images' z-stacks, with 10 measurements in each category per depth. Then, measurements were averaged for each category and linear functions between them were calculated to normalize the data in a singular dataspace.

To analyze tau staining intensity along the blood vessel, the exported coordinates were input into a script that calculates the pixel distance, in microns, along the surface of the blood vessel. This script calculated a centerline through the blood vessel, found the nearest position on the centerline to each tau pixel, and calculated that position's distance from the start of the centerline [11]. The data were then exported as the original coordinates with their distance along the vessel appended. A similar script was used for the neuron and tangle density analysis, where the object coordinates obtained from Ilastik were input along with the intensity coordinates. This script calculated the distance along the vessel for each object within 30 microns of the vessel surface.

Finally, these data were binned into groups based on their distance along and away from the blood vessel. Immunolabeling intensity, neuron, and NFT data were grouped in 10-micron intervals along the vessel surfaces. For tau intensity, the mean intensity was calculated for each bin, and data within 3 microns from each vessel surface was used to determine the surface tau percentile [25]. For neurons and tangles, their density was calculated by measuring the number of objects within 30 microns from the vessel surface and comparing their quantity to the spatial volume of each bin. Last, mean tau intensity was normalized to control samples, and R Studio software was used to create heatmaps of tau intensity as a function of vessel surface distance (μm).

Statistical analysis

All statistical analysis was performed in GraphPad Prism (version 10.2.2). For comparisons with two groups, Shapiro–Wilks normality tests were applied followed by two-tailed Student's *t* tests or Mann–Whitney *U* tests. A priori, an outlier test (ROUT; Graphpad Prism) was used to assess the biochemical data and no outliers were detected—all data have subsequently been included. A repeated-measures ANOVA was used to examine the association between tau intensity along blood vessels and nearby tangle density. In all cases, statistical significance was defined as $p < 0.05$.

Results

Three-dimensional histology reveals the accumulation of tau protein along blood vessels

Tissue was collected from the inferior temporal gyrus, a region associated with functional impairment and tau accumulation in AD [16]. Each block was sliced into 0.5–1 mm thick sections, then cleared and immunolabeled following an optimized protocol described previously [45]. AD and control human brain tissue samples were immunolabeled for phospho-tau (AT8, recognizes tau phosphorylated at both S202 and T205), blood vessels (Glut1), neurons (HuD), and cell nuclei (DAPI, Fig. 1a–b) [9, 12, 13, 23].

Visual inspection of vasculature reveals significant phospho-tau staining along the surface of some blood vessels (Fig. 1c–e). This phospho-tau staining is distinct from neurofibrillary tangles and shows a diffuse pattern that appears regionally along the length of select blood vessels in each sample. Control samples (Braak 0-I) did not have neurofibrillary tangles or phospho-tau + staining along blood vessels (Fig. 1b, f). In segments with vascular tau staining, staining also appears to extend away from the blood vessel surface and diminish as distance increases from the surface (Fig. 1c, d). Additionally, select blood vessels showed the accumulation of adjacent NFTs in addition to the diffuse staining on their surface (Fig. 1e). These observations suggest a spatial relationship between vasculature and phosphorylated tau accumulation in AD that is distinct from NFTs.

Characteristics, cortical location, and CAA status of blood vessels with tau accumulation

To better define vascular tau, we established a protocol for isolating, quantifying, and classifying regions of tau accumulation on blood vessels. The virtual reality (VR) image analysis software Syglass was used to manually segment individual blood vessels from each sample by tracing masks along the surface of each blood vessel (Fig. 2a). We found that VR tracing allowed us to more efficiently and accurately segment individual vessels compared to segmentation on 2D planes. Individual vessel masks were then realigned to the original image coordinates to quantify staining in other channels. In total, we segmented 16–26 blood vessels from $n = 6$ AD and $n = 6$ control donor brains (Table 1). Of note, none of the samples included in this study had CAA type 1 or age-related tau astrogliopathy (ARTAG)[24] in any brain region assessed by the ADRC, or evidence of cardiovascular disease (CVD)-related changes (including infarcts) in the region of inferior temporal cortex selected for this study.

Using these vessel masks, we next examined the characteristics and cortical location of individual tau-positive vessels. We subdivided each image into its respective layers and found that the average tau intensity on the blood vessel surface—defined as the region within 3 microns of the vessel mask—was distributed across all cortical layers except for layer 6 (Fig. 2b). This distribution pattern is distinct from the amount of tangles and neurons present in each cortical region (Fig. 2c, d). Vascular tau was not observed along microvessels (< 10 μm in diameter), and the average diameter of measured vessels was 17 μm ± 4 (std. dev.). Vessels of similar size were selected for comparison in control tissues (Fig. 2e). Further, we also examined whether vessels with tau accumulation were arterial or venous using co-labeling

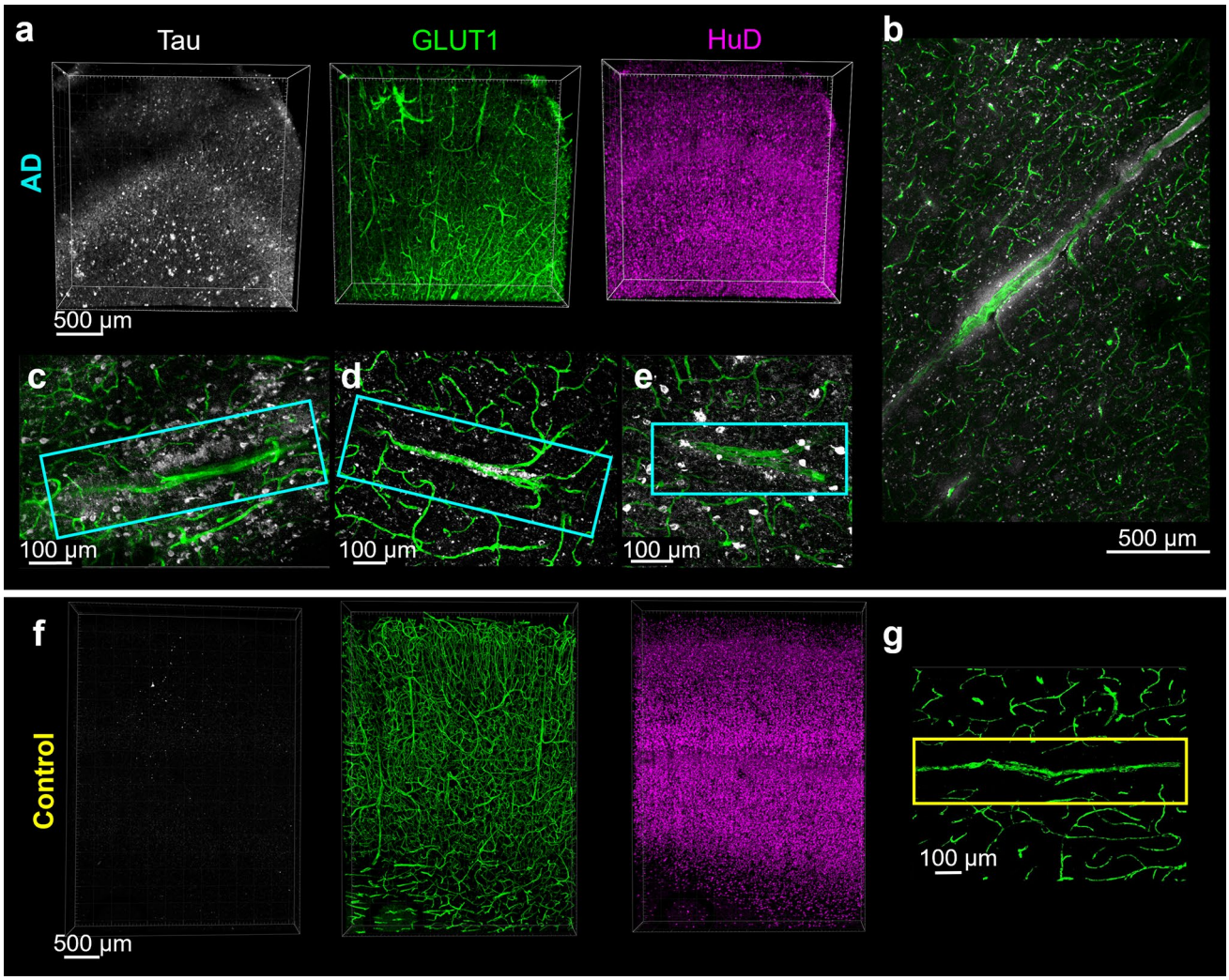

Fig. 1 Three-dimensional histology reveals the presence of vascular-associated tau. Confocal fluorescence microscopy images showing raw data from the inferior temporal gyrus of AD donors (**a**–**e**) or a control (**f**, **g**). **a** Overview images of thick tissue immunolabeled for AT8 tau (white), vasculature (GLUT1, green) and neurons (HuD, magenta). **b**–**e** Examples of vascular tau accumulation (white) around blood vessels (green) from four different AD donors. **f** Overview images of thick tissue from a control donor immunolabeled as in panel A. Note the absence of tau labeling. **g** Example image of a comparable tau-negative blood vessel (green) from a control donor. Images from C–E and F show 40 µm thick z-slices

with smooth muscle actin (SMA, a marker of smooth muscle cells; Fig. 2f) and confirmed their identity as arterioles.

Finally, a separate set of tissue slices was labeled for amyloid beta in addition to tau and blood vessels to determine whether tau co-occurs with CAA. In 3 of 6 donors used for vascular tau quantification, no CAA-positive vessels were observed. Of the remaining three, two had occasional CAA-positive leptomeningeal vessels and these vascular segments were not tau-positive (Fig. 3a, b, d; Supplementary Movie 1). However, in the remaining donor tissue, severe CAA pathology was observed including in the penetrating arterioles. In this case, amyloid-laden blood vessels were also observed to have enhanced vascular tau labeling (Fig. 3c, e). Interestingly, this donor was the only known homozygous *APOE4* carrier. Thus, while tau-positive vessels appear to be largely separate from CAA including in their distribution throughout the cortex, we note some overlap.

Frequency of vascular tau accumulation in inferior temporal gyrus

Next, we measured the intensity of tau labeling along the vascular surface. Each measured vessel had a segmented length that was continuous for roughly 300–2000 microns (Fig. 4a). Control samples consistently lacked tau accumulation along any blood vessels. There was also substantial diversity in the pattern of tau along blood vessels, both within and across AD samples. To simplify comparisons

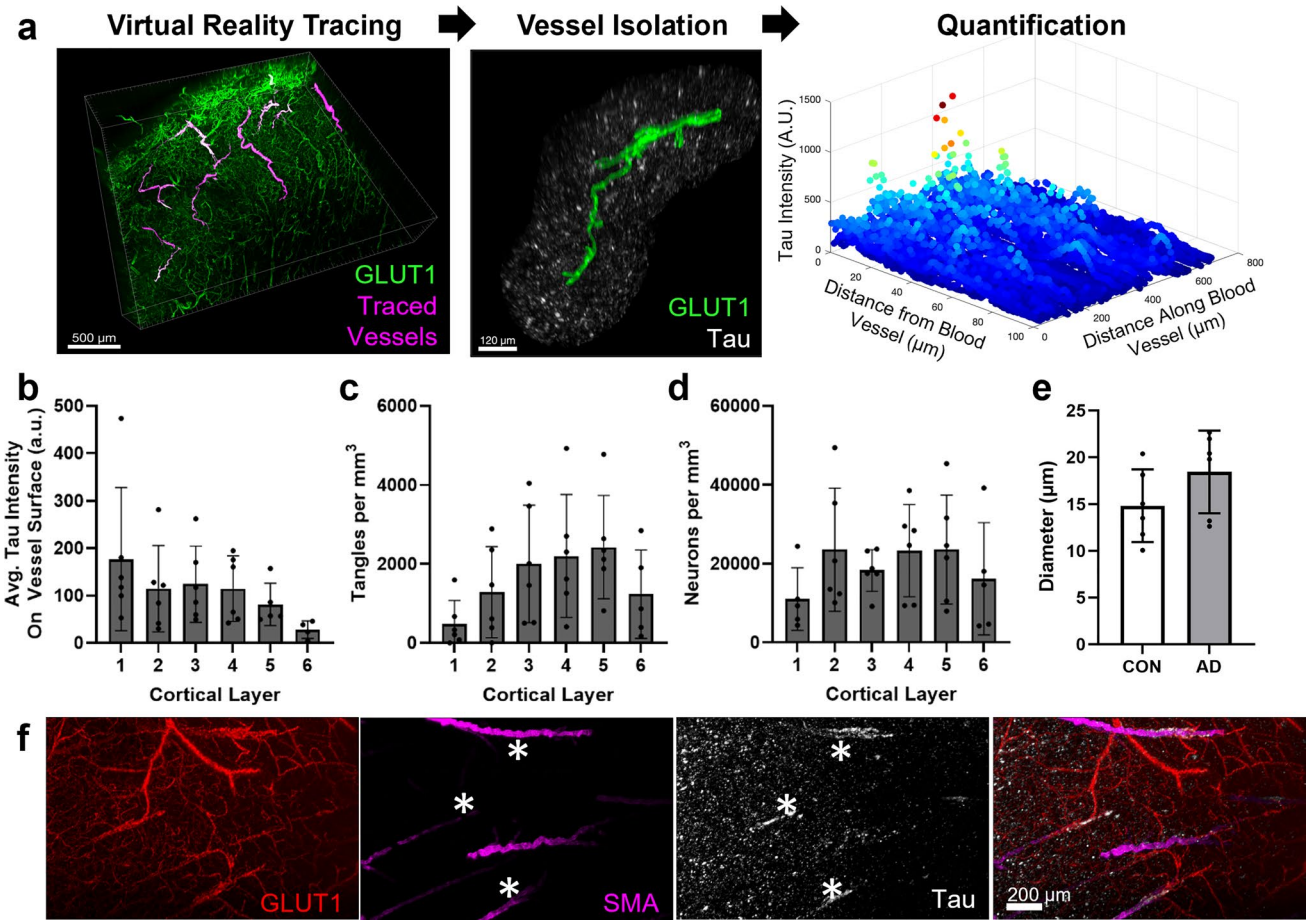

Fig. 2 Examination of tau along individual blood vessels throughout the cortex. **a** An overall schema of the method used to quantify vascular tau. Blood vessels are first traced in virtual reality (magenta) and are shown overlying the original GLUT1-positive blood vessel imaging data (green). Tracing allows for the isolation of individual blood vessels and their surround, including tau pathology (white) ≤ 100 µm from the blood vessel surface (example is from AD 5 vessel 5). Subsequently, quantification of tau intensity along and away from the blood vessel surface was conducted. **b** Measures of the average tau intensity at the vessel surface (within 3 microns) per donor and cortical layer. Each dot represents the average of several measures along the length of individual vessels per donor (see Fig. 4B). **c** The average AT8-positive tangle density and (**d**) HuD-positive neuron density per cubic mm were also measured for each cortical layer. **e** The average diameter of vessels measured per donor. Dots represent individuals, bars represent means ± SEM. **f** Separate tissue labeled with antibodies to GLUT1, SMA, and tau show areas of tau accumulation on blood vessels that are also SMA-positive (indicated by asterisks)

of tau accumulation across samples, we subdivided each 10-micron interval along a vessel surface into segments and assigned each segment a percentile based on the average phospho-tau staining intensity within that segment (Fig. 4b). Regions of tau accumulation included stretches spanning small vascular lengths of < 50 microns to > 1000 microns and could appear continuous or patchy (Fig. 4c–h).

We hypothesized that one potential explanation for these observations could be that vessels occasionally travel through regions of high tau pathology. To rule out that the appearance of tau is coincidental, we compared differences between groups of vascular segments within each percentile bin. Segments with the most vascular tau (top 90–100 percentiles) show substantial increase in tau intensity near the vessel that decreases with distance from the vessel surface (Fig. 5). This indicates that tau is enriched near blood vessels compared to the surrounding tissue. By comparison, segments in the next decile (80–90th percentiles) show no substantial change in tau intensity with distance from the vessel surface, indicating no enrichment. Segments with less surface tau (80th percentile and below) show the opposite trend—a decrease in tau intensity near the vessel surface (Fig. 5). These data indicate that tau immunolabeling is generally lower near blood vessels, but in a subset of vascular regions tau burden is enhanced compared to the surrounding tissue. Together, this strongly supports the idea that vascular tau is spatially distinct from tau in other compartments.

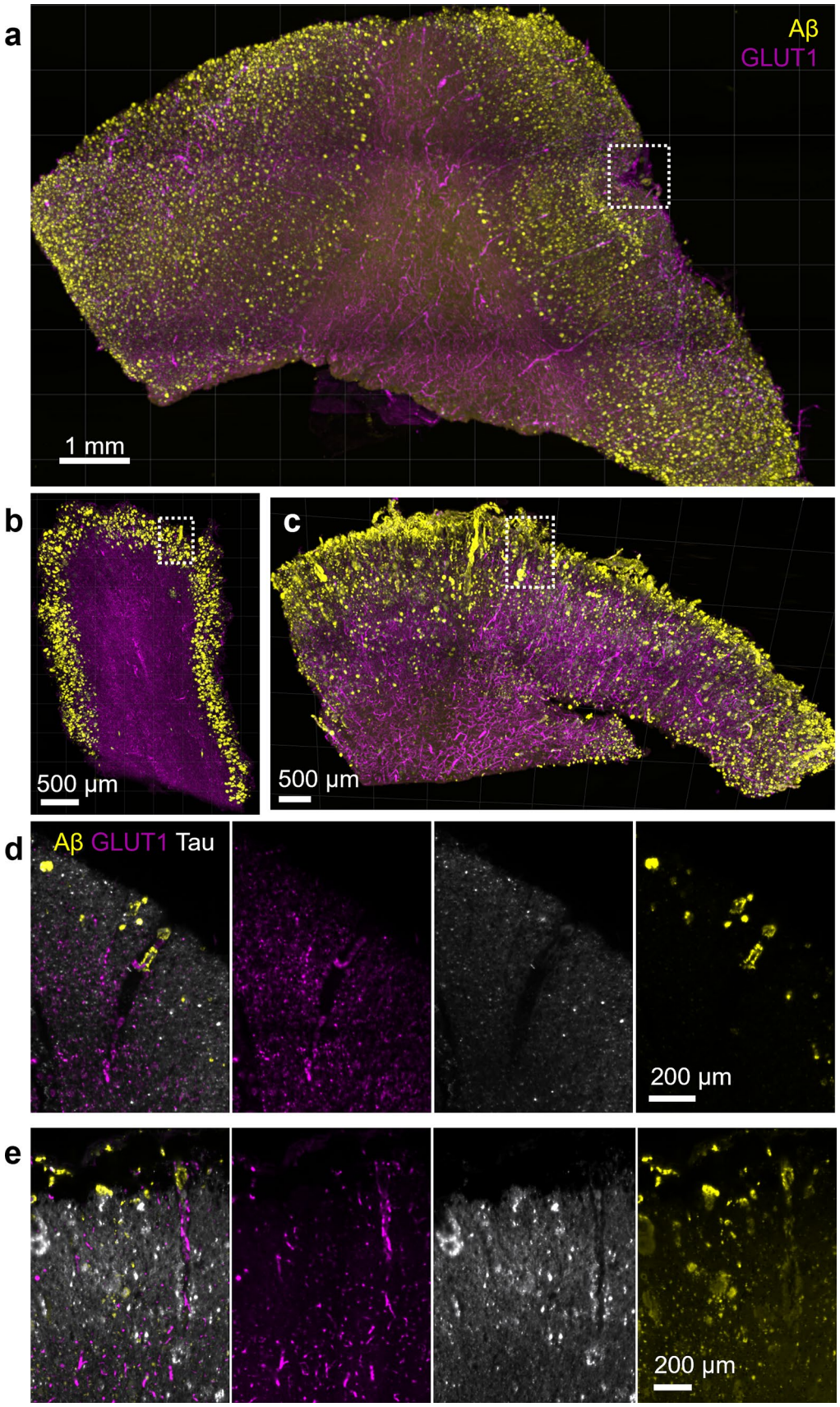
a
Aβ
GLUT1
1 mm
b
500 µm
c
500 µm
d
Aβ GLUT1 Tau
200 µm
e
200 µm

◂**Fig. 3** CAA pathology and tau accumulation. **a** Tissue from donor AD 6 shows areas with leptomeningeal CAA pathology. An additional view of the area in the dashed box is shown in Supplementary Movie 1. **b** Tissue from donor AD 5 shows a rare CAA-positive vessel. Closeup of the dashed box shown in panel d. **c** Frequent CAA-positive vessels were observed in donor AD 1. A closeup of the region in the dashed box is shown in panel. **e** A region of a CAA-positive vessel with tau accumulation is indicated by the red arrow

Composition of tau in blood vessels

Pathological tau is heavily post-translationally modified, so we additionally sought to understand what forms of tau are present in this vascular compartment by physically isolating blood vessels from the ITG of our AD and control samples and conducting capillary Western immunoassays (Fig. 6a). The assays revealed a significant increase total tau, the tau N-terminus (Tau13), and phospho-T181 and -T217 tau in the blood vessels of AD donors compared to controls (Fig. 6b, c, e, g). Incubation of blood vessels alone with tau-containing homogenate was not sufficient to result in enrichment, confirming that this enhanced tau in the vascular compartment is not due to the isolation procedure (Supplementary Fig. 1). By comparison, the levels of other forms of tau, S202, P231, and the tau C-terminus (Tau46), were not found at significantly higher levels in AD samples compared with controls (Fig. 6d, f, h). In total, this indicates that the enrichment of tau in vasculature is not an artifact of the AT8 antibody and that certain forms of tau are increased in this compartment in AD.

Relationship between vascular tau and NFT burden

Given the enrichment in vasculature of tau species known to contribute to the formation of NFTs, and an observation that tangles in AD tissues were frequently adjacent to tau-positive vessels (Fig. 7a–d), we next wanted to understand if areas of increased vascular tau were related to the local NFT burden. To do this, we segmented individual NFTs and neurons in our images (Fig. 7e–g). We then calculated the percent of neurons containing NFTs near blood vessels to determine the relationship between the amount of vascular surface tau and the likelihood of nearby neurons being NFT-positive. This quantification was done in the tissue immediately adjacent to the blood vessel—defined as a volume within 30 microns of the vessel surface. An ANOVA, correcting for repeated measures, shows a significant difference in the percent of neurons with NFTs that varies with vascular surface tau percentile ($p = 0.037$, $R^2 = 0.47$; Fig. 7h). This indicates the number of nearby neurons with NFTs increases as vascular surface tau increases.

Discussion

Tau accumulation and NFT formation are closely associated with the clinical progression of Alzheimer's disease [2]. Here, we report that the accumulation of tau along blood vessels is apparent in three-dimensional histology. These experiments indicate that pathological tau exhibits a close spatial relationship to vasculature in human Alzheimer's disease brain. This provides evidence of an interaction between tau pathology and blood vessels, perhaps similar to CAA. Such an interaction reinforces previous studies conducted in mouse models of tau pathology which found changes in cerebral microvessels [5, 6, 31]. These results also provide further evidence for the existence of a vascular clearance pathway for tau pathology, which may be disrupted in regions with increased levels of tau accumulation.

Recent studies have investigated the role of vasculature in tau clearance at larger, systemic scales in mouse models of AD, finding that brain vasculature and the associated glymphatic system regulate clearance of tau pathology [18, 20, 22]. These conclusions have been supported in human magnetic resonance imaging, where perivascular spaces were found to be associated with tau pathophysiology in early AD [40]. Our study investigated the association of tau and vasculature at smaller, single-cell spatial scales in human AD donors to determine if patterns of tau accumulation are consistent with the observations of these previous studies. Indeed, the large-volume images we obtained of the inferior temporal gyrus indicate that tau accumulates along vascular segments in AD, suggesting that the clearance of tau pathology by vasculature may be dysfunctional in this area. Specifically, we found that some blood vessels exhibit regions with higher levels of tau near the blood vessel surface than the surrounding tissue—indicating that tau positivity is not simply occurring by chance. In areas with low levels of vascular tau, tau intensity is lower near the vessel surface compared to its surroundings, suggesting functional vascular clearance. Altogether these data support the idea that vessels are important for tau clearance in AD.

The deposition of tau on blood vessels is similar to CAA, but our data suggests that these are a distinct phenomenon. Tau-positive vessels are primarily arterioles. However, leptomeningeal vessels were not observed to be sites of tau deposition, with areas of tau-positive vessels being distributed throughout cortical layers I–V. By comparison, CAA type 2-affected vessels are frequently found in the leptomeninges and arterioles in superficial cortical layers [37, 41]. CAA-affected vessels from two donor tissues used in this study did not coincide with tau-positive segments. In contrast, in one *APOE4/4* donor, we observed frequent CAA vessels that also had evidence of tau deposition. This is in line with prior studies that have reported that neuritic

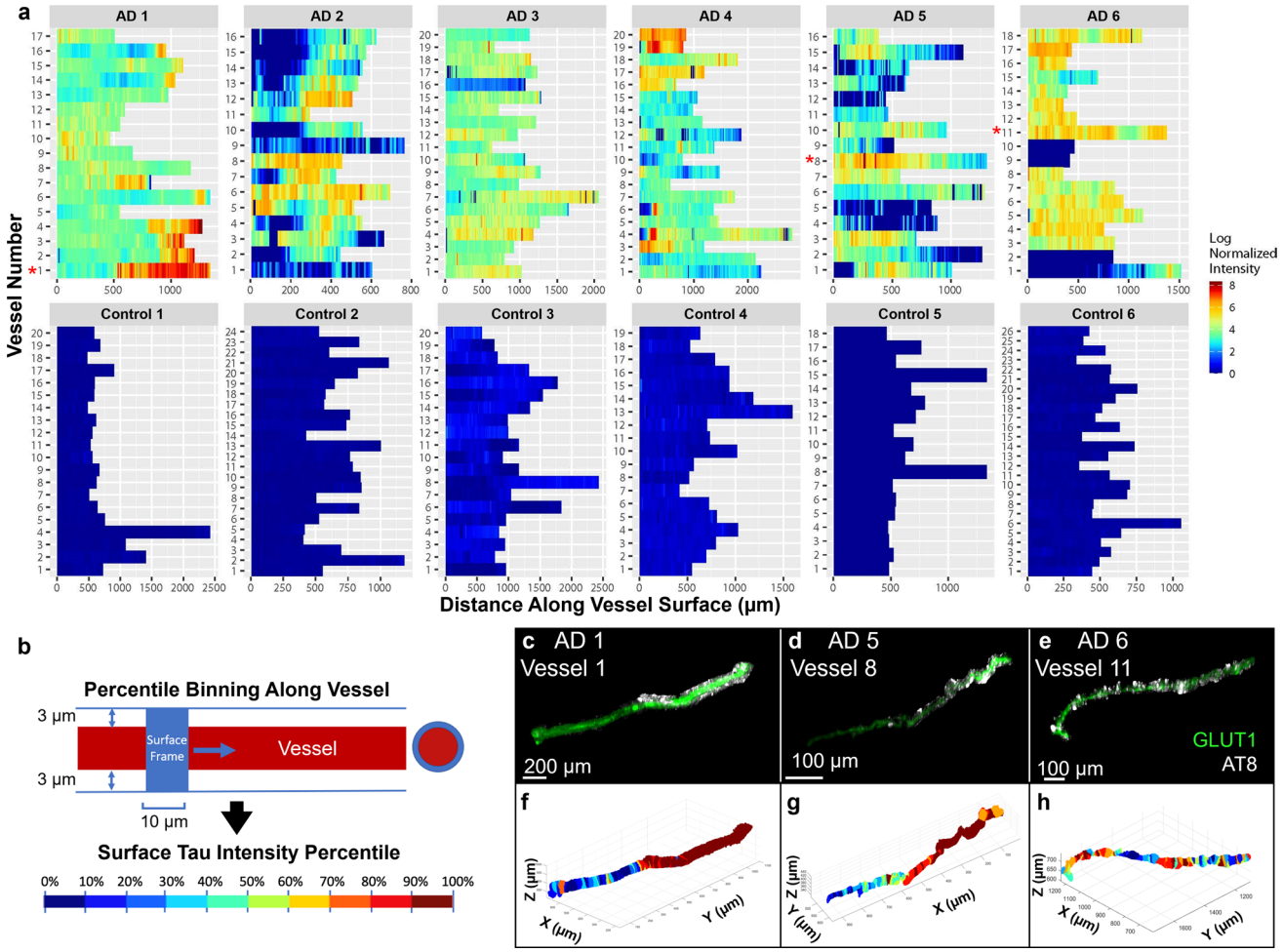

Fig. 4 Mapping tau accumulation on blood vessels. **a** Heatmaps showing log normalized tau intensity within 3 microns from the surface of each segmented blood vessel ($n = 107$ AD, $n = 127$ control). Rows are individual vessels and columns are tau intensity measures along the vessel length. Red asterisks highlight example vessels shown in panels C–H. **b** Data are binned every 10 microns along the blood vessel's surface and shows the mean intensity of each bin, normalized to the mean tau intensity of the whole image. **c**, **d**, **e** Example of isolated blood vessel (green) and tau labeling (white). **f**, **g**, **h** Corresponding maps of tau intensity along the vessel surface. Color corresponds to percentiles (deciles)

dystrophies are increased near vessels that accumulate CAA [30, 39]. Tau positivity also did not appear to overlap with dyshoric capillary changes, though cases with CAA type 1 were not included in this study [33]. Other CAA-related features we did not observe in tau-positive segments included vessels with a "double-barrel" appearance or the presence of microhemorrhages. In sum, while we cannot rule out that some tau-positive vessels may also be affected by CAA at other locations along their length, the majority of vessels assessed in this study did not appear to also have amyloid beta accumulation.

Furthermore, we performed protein assays that found blood vessels in AD patients contain higher levels of N-terminal tau and phospho-tau species compared to controls. Prior analyses of CSF from AD donors reported an enrichment for N-terminal fragments versus controls, in line with these observations [10, 35]. Additionally, we observed increased phospho-T217 in AD blood vessel isolates. Phospho-T217 tau is a sensitive blood-based biomarker for AD and a form of phosphorylated tau found to accumulate in AD and drive the hyperphosphorylation and fibrillization of wild-type tau [15, 43]. This suggests that blood vessels harbor aggregate-prone species of tau, which was further supported by analysis showing an association between vascular tau and local NFT density. These data align with previous reports that observed a greater incidence of tau labeling near vessels with increasing Braak stage and our own prior work showing that isolated blood vessels from AD brain are enriched for tau species capable of seeding new aggregates [5, 29]. We also note that in this work, vascular enrichment of tau was observed in a Braak III donor with AD and limited temporal cortex NFT accumulation,

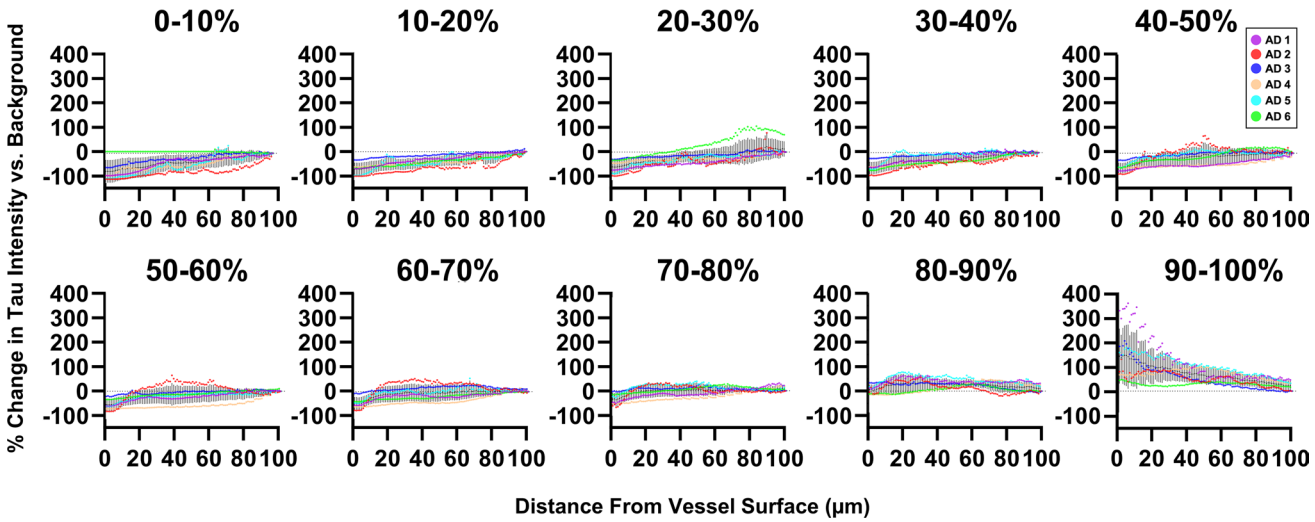

Fig. 5 Tau intensity is related to distance from the blood vessel surface. Blood vessel segments (10-micron bins, as shown in Fig. 4b) were grouped according to surface tau intensity by percentiles (deciles). The relative change in tau immunolabeling near these vessel segments was plotted as a function of distance from blood vessel surface. To allow comparison between donor samples, the values for each donor (colored coded) are normalized to the average tau intensity value in the whole image (background) such that a 0% change (gray dashed line) means the vascular tau labeling intensity is no different than the average intensity of tau in the whole image. Vessel segments in the top decile (90–100%) show greater than background tau intensity near the vessel surface whereas other deciles reduced or no difference in intensity near the vessel surface. Each point represents a measure at 1-micron intervals. Gray vertical bars indicate SEM

further hinting at involvement of blood vessels in early disease. Prominent accumulation of NFTs near blood vessels is also a neuropathological feature of the mildest forms of chronic traumatic encephalopathy in young individuals and this may indicate shared mechanisms between diseases [27, 28]. Together, these observations suggest that impaired vascular clearance of tau may contribute to the progression of AD pathology though further evaluation of early AD changes (and other brain regions) would help to clarify this relationship.

In addition to the experimental results of our study, we also present a new methodology for characterizing disease pathology relative to anatomical structures. Until recently, it has not been possible to image large tissue volumes with cellular and sub-cellular resolution, but new imaging methods, such as confocal and light sheet fluorescence microscopes, coupled with tissue clearing technology have now enabled this. However, many of the current, most widely used quantification tools face challenges analyzing these images, as they were primarily designed for traditional, two-dimensional analysis [3, 34]. This study presents a method utilizing emerging machine learning and virtual reality tracing software to identify objects throughout large images, while accounting for differential staining and object characteristics throughout the image volume, a challenge that traditional simple thresholding and rolling-ball filtering methods do not account for. This is a significant development, because it allows for the alignment of pathology, brain structures, and original imagery to investigate spatial relationships across large regions, while maintaining cellular resolution.

While these data indicate that tau is enriched at points along blood vessels compared to the surrounding tissue, additional characterization, including studies with sub-cellular resolution of tau-enriched vessels, is needed to better understand the cause and consequence of this buildup on blood vessels. For example, studies have implicated aquaporin 4 (AQP4) in the clearance of tau; thus, AQP4 provides a possible target for studies looking to determine the precise cause of vascular tau [14]. If specific transporters or tau-interacting proteins can be identified, they may offer a new target for therapeutics designed to remove tau pathology. Further, while nearly all vessels examined in AD inferior temporal gyrus exhibited regions of enhanced tau accumulation, this study was restricted to a single cortical region in a small number of AD donors, limiting our power to explore additional variables. Whether these findings can be extended to other brain areas, including those where NFTs are relatively scant such as the visual cortex and cerebellum, and how vascular accumulation may be modified *APOE* genotype, sex, and co-morbid conditions such as CVD (including hypertension) could widen our understanding of this phenotype. Last, the control donors used for quantitative assessment of vascular tau were relatively young compared to the AD group, and there may be additional age-related vascular tau accumulation that was not directly visualized in this study.

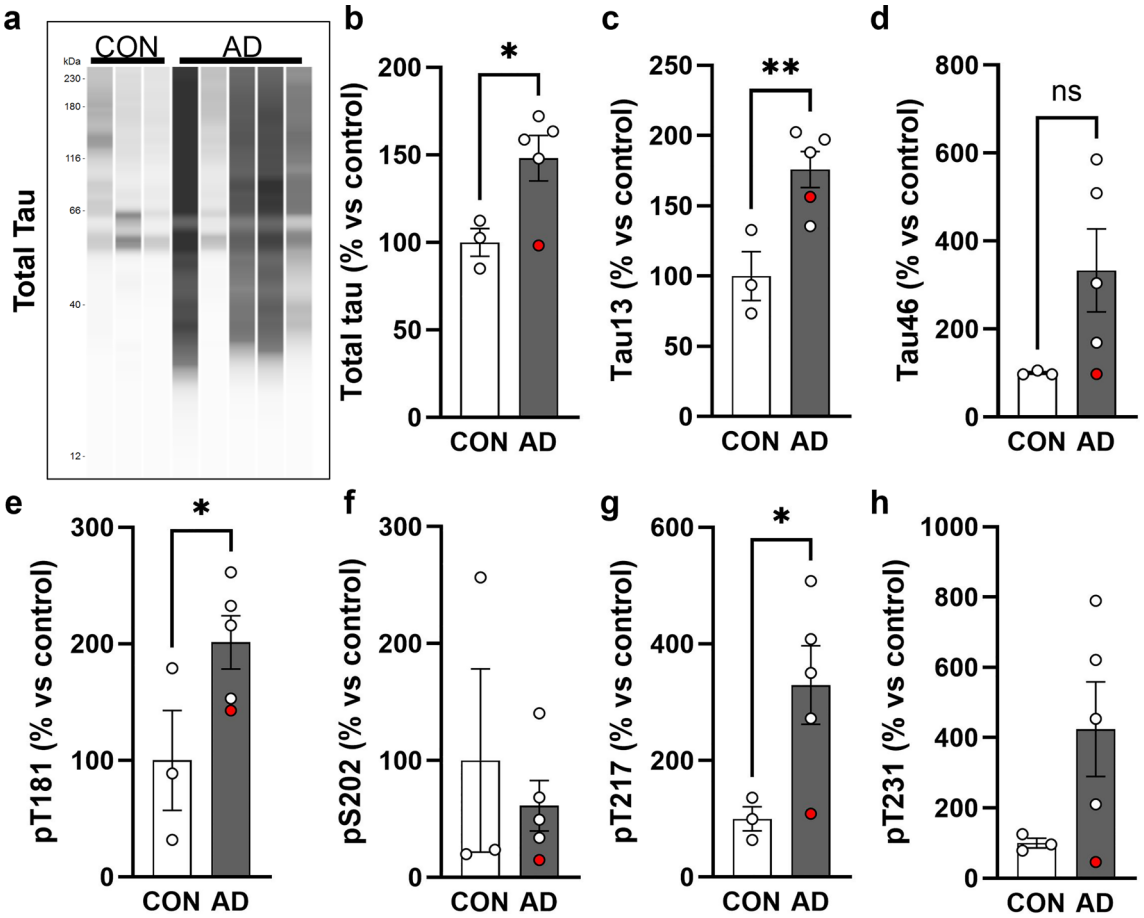

Fig. 6 Post-translationally modified tau is enriched in AD blood vessels. **a** Isolation of blood vessels from the inf. temp. gyrus of $n=3$ control and $n=5$ AD brains shows that tau is enriched in vasculature and can be visualized with multiple antibodies including total tau = DAKO rabbit polyclonal. Quantification of total signal per lane for (**b**) total tau, (**c**) Tau13 n-terminal antibody, (**d**) Tau46 c-terminal antibody, (**e**) phospho-T181 tau, (**f**) phospho-S202 tau, (**g**) phospho-T217 tau and (**h**) phospho-T231 tau. The AD donor that is Braak III is labeled in red. All values normalized to the average of controls. One-tailed t-test $*p<0.05$, $**p<0.01$. Error bars = means ± SEM

In summary, this study provides new evidence of brain vasculature's role in the progression of AD and distribution of pathology. Perhaps most notably, our results indicate that tau deposits around vasculature with characteristics similar to amyloid beta in CAA. Additionally, this work provides further support for the role of vasculature in mediating tau clearance. Future investigation of how this disrupts vascular functions including specific transporter mechanisms in endothelial cells, may help uncover new

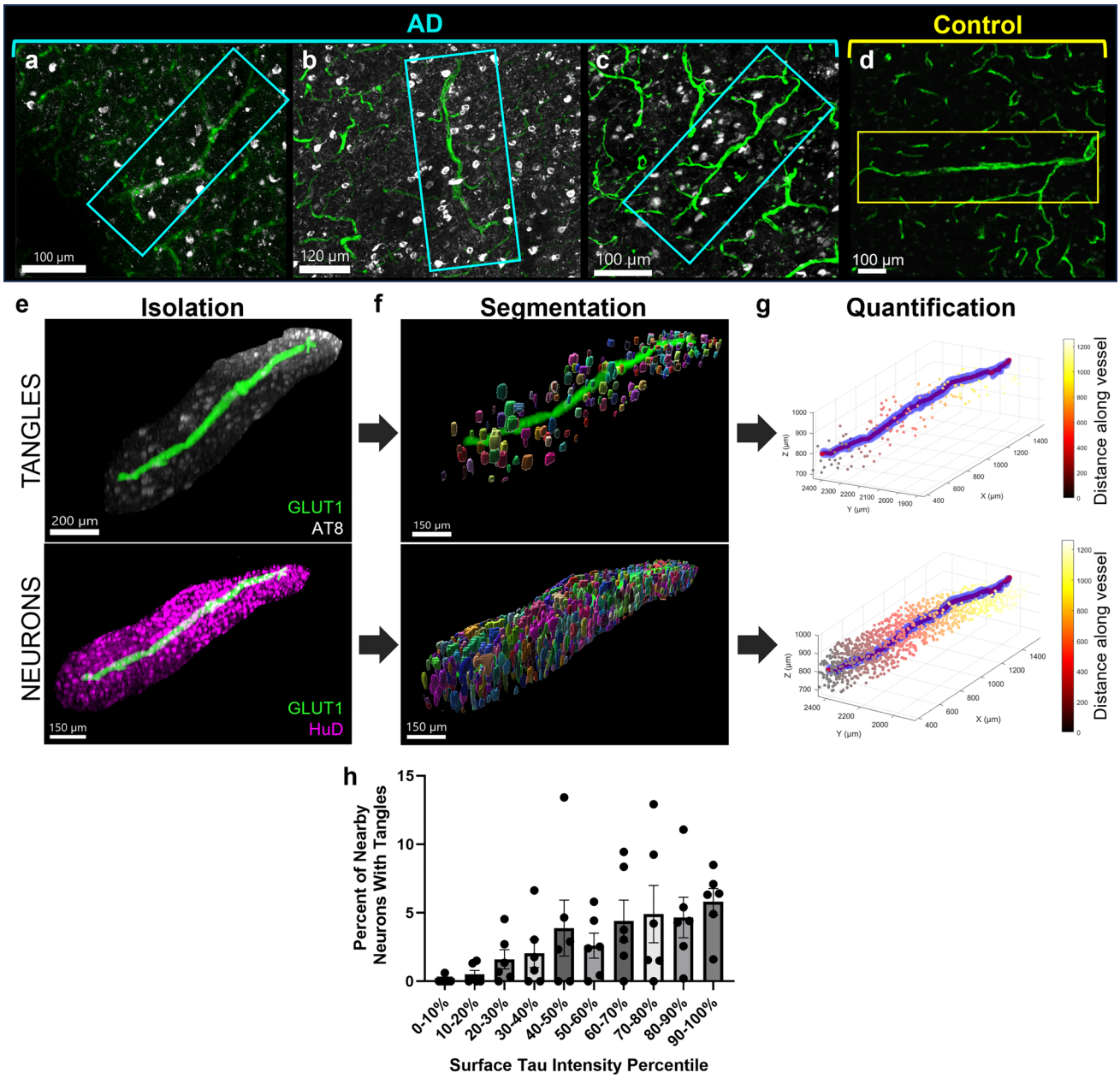

Fig. 7 NFT and neuron density analysis. Examples of blood vessels showing NFT accumulation near the blood vessel surface in samples (**a**) AD 2, (**b**) AD 1, (**c**) AD 6, and (**d**) control 3. **e** Isolated blood vessel with surrounding tau pathology (AT8, white) and surrounding neurons (HuD, magenta). **f** NFTs and neurons were identified and segmented using Ilastik. A visualization of segmentation masks was generated using Imaris and with a value of 1 µm to smooth the surfaces. **g** A custom MATLAB script was developed to calculate the distance of each segmented tangle and neuron from the surface of each blood vessel. Plots show the blood vessel (blue), its calculated centerline for object distance calculations (red), and objects colored according to their distance along the blood vessel. **h** Plot shows the percent of neurons with NFT in regions near (0–30 microns) blood vessels with varying amounts of surface tau. Repeated measures ANOVA $p = 0.037$, $R^2 = 0.47$. Dots represent individuals, bars represent means ± SEM

methods to modify tau burden in the brain via vascular clearance.

Supplementary Information The online version contains supplementary material available at https://doi.org/10.1007/s00401-024-02751-9.

Acknowledgements We additionally thank the donors and their families who have contributed to the Massachusetts Alzheimer's Disease Research Center, which is supported by the NIH NIA P30AG062421. We would also like to thank the Harvard Center for Biological Imaging including Douglas Richardson for the use of their imaging facility and helpful conversations and the Alzheimer's Clinical and Translational

Research Unit and their Data Visualization team at MGH for use of their virtual reality systems.

Funding This work was supported by a grant from the Alzheimer's Association (23AARG-1029355; REB), by the NIH NIA R00AG068602 (TJZ) and R00AG061259 (REB), the Harrison Gardner Jr Innovation Award (BTH, TJZ), the Jack Satter Foundation (BTH, REB, TJZ), and a Predoctoral Fellowship FPU18/00630 from the Spanish Ministry of Science, Innovation, and Universities (ES).

Data availability The data underlying this article will be shared on reasonable request to the corresponding author.

Declarations

Conflict of interest BTH has a family member who works at Novartis and owns stock in Novartis; he serves on the SAB of Dewpoint and owns stock. He serves on a scientific advisory board or is a consultant for AbbVie, Avrobio, Axon, Biogen, BMS Cell Signaling, Genentech, Ionis, Novartis, Seer, Takeda, the US Dept of Justice, Vigil, Voyager. His laboratory is supported by Sponsored research agreements with AbbVie, F Prime, and research grants from the Cure Alzheimer's Fund, Tau Consortium, and the JPB Foundation. REB works on the AbbVie-Hyman Collaboration. The other authors declare no competing interests.

References

1. Arnold SE, Hyman BT, Flory J, Damasio AR, Van Hoesen GW (1991) The topographical and neuroanatomical distribution of neurofibrillary tangles and neuritic plaques in the cerebral cortex of patients with Alzheimer's disease. Cereb Cortex 1:103–116. https://doi.org/10.1093/cercor/1.1.103
2. Arriagada PV, Growdon JH, Hedley-Whyte ET, Hyman BT (1992) Neurofibrillary tangles but not senile plaques parallel duration and severity of Alzheimer's disease. Neurology 42:631–639. https://doi.org/10.1212/wnl.42.3.631
3. Bankhead P, Loughrey MB, Fernandez JA, Dombrowski Y, McArt DG, Dunne PD et al (2017) QuPath: open source software for digital pathology image analysis. Sci Rep 7:16878. https://doi.org/10.1038/s41598-017-17204-5
4. Barthelemy NR, Saef B, Li Y, Gordon BA, He Y, Horie K et al (2023) CSF tau phosphorylation occupancies at T217 and T205 represent improved biomarkers of amyloid and tau pathology in Alzheimer's disease. Nat Aging 3:391–401. https://doi.org/10.1038/s43587-023-00380-7
5. Bennett RE, Hu M, Fernandes A, Perez-Rando M, Robbins A, Kamath T et al (2020) Tau reduction in aged mice does not impact microangiopathy. Acta Neuropathol Commun 8:137. https://doi.org/10.1186/s40478-020-01014-4
6. Bennett RE, Robbins AB, Hu M, Cao X, Betensky RA, Clark T et al (2018) Tau induces blood vessel abnormalities and angiogenesis-related gene expression in P301L transgenic mice and human Alzheimer's disease. Proc Natl Acad Sci U S A 115:E1289–E1298. https://doi.org/10.1073/pnas.1710329115
7. Berg S, Kutra D, Kroeger T, Straehle CN, Kausler BX, Haubold C et al (2019) ilastik: interactive machine learning for (bio) image analysis. Nat Methods 16:1226–1232. https://doi.org/10.1038/s41592-019-0582-9
8. Bierer LM, Hof PR, Purohit DP, Carlin L, Schmeidler J, Davis KL et al (1995) Neocortical neurofibrillary tangles correlate with dementia severity in Alzheimer's disease. Arch Neurol 52:81–88. https://doi.org/10.1001/archneur.1995.00540250089017
9. Bronicki LM, Jasmin BJ (2013) Emerging complexity of the HuD/ELAVl4 gene; implications for neuronal development, function, and dysfunction. RNA 19:1019–1037. https://doi.org/10.1261/rna.039164.113
10. Cicognola C, Brinkmalm G, Wahlgren J, Portelius E, Gobom J, Cullen NC et al (2019) Novel tau fragments in cerebrospinal fluid: relation to tangle pathology and cognitive decline in Alzheimer's disease. Acta Neuropathol 137:279–296. https://doi.org/10.1007/s00401-018-1948-2
11. D'Errico J (2024) arclength. MATLAB Central File Exchange. https://www.mathworks.com/matlabcentral/fileexchange/34871-arclength. Accessed 12 Jun 2024
12. Gerhart DZ, LeVasseur RJ, Broderius MA, Drewes LR (1989) Glucose transporter localization in brain using light and electron immunocytochemistry. J Neurosci Res 22:464–472. https://doi.org/10.1002/jnr.490220413
13. Goedert M, Jakes R, Vanmechelen E (1995) Monoclonal antibody AT8 recognises tau protein phosphorylated at both serine 202 and threonine 205. Neurosci Lett 189:167–169. https://doi.org/10.1016/0304-3940(95)11484-e
14. Gomolka RS, Hablitz LM, Mestre H, Giannetto M, Du T, Hauglund NL et al (2023) Loss of aquaporin-4 results in glymphatic system dysfunction via brain-wide interstitial fluid stagnation. Elife. https://doi.org/10.7554/eLife.82232
15. Groot C, Cicognola C, Bali D, Triana-Baltzer G, Dage JL, Pontecorvo MJ et al (2022) Diagnostic and prognostic performance to detect Alzheimer's disease and clinical progression of a novel assay for plasma p-tau217. Alzheimers Res Ther 14:67. https://doi.org/10.1186/s13195-022-01005-8
16. Halawa OA, Gatchel JR, Amariglio RE, Rentz DM, Sperling RA, Johnson KA et al (2019) Inferior and medial temporal tau and cortical amyloid are associated with daily functional impairment in Alzheimer's disease. Alzheimers Res Ther 11:14. https://doi.org/10.1186/s13195-019-0471-6
17. Hansson O, Zetterberg H, Buchhave P, Londos E, Blennow K, Minthon L (2006) Association between CSF biomarkers and incipient Alzheimer's disease in patients with mild cognitive impairment: a follow-up study. Lancet Neurol 5:228–234. https://doi.org/10.1016/S1474-4422(06)70355-6
18. Harrison IF, Ismail O, Machhada A, Colgan N, Ohene Y, Nahavandi P et al (2020) Impaired glymphatic function and clearance of tau in an Alzheimer's disease model. Brain 143:2576–2593. https://doi.org/10.1093/brain/awaa179
19. Hyman BT, Phelps CH, Beach TG, Bigio EH, Cairns NJ, Carrillo MC et al (2012) National Institute on Aging-Alzheimer's Association guidelines for the neuropathologic assessment of Alzheimer's disease. Alzheimers Dement 8:1–13. https://doi.org/10.1016/j.jalz.2011.10.007
20. Iliff JJ, Chen MJ, Plog BA, Zeppenfeld DM, Soltero M, Yang L et al (2014) Impairment of glymphatic pathway function promotes

tau pathology after traumatic brain injury. J Neurosci 34:16180–16193. https://doi.org/10.1523/JNEUROSCI.3020-14.2014
21. Iliff JJ, Wang M, Liao Y, Plogg BA, Peng W, Gundersen GA et al (2012) A paravascular pathway facilitates CSF flow through the brain parenchyma and the clearance of interstitial solutes, including amyloid beta. Sci Transl Med. https://doi.org/10.1126/scitranslmed.3003748
22. Ishida K, Yamada K, Nishiyama R, Hashimoto T, Nishida I, Abe Y et al (2022) Glymphatic system clears extracellular tau and protects from tau aggregation and neurodegeneration. J Exp Med. https://doi.org/10.1084/jem.20211275
23. Kapuscinski J (1995) DAPI: a DNA-specific fluorescent probe. Biotech Histochem 70:220–233. https://doi.org/10.3109/10520299509108199
24. Kovacs GG, Ferrer I, Grinberg LT, Alafuzoff I, Attems J, Budka H et al (2016) Aging-related tau astrogliopathy (ARTAG): harmonized evaluation strategy. Acta Neuropathol 131:87–102. https://doi.org/10.1007/s00401-015-1509-x
25. Lal Shrestha D (2023) Percentiles of a sample. City
26. Lewis DA, Campbell MJ, Terry RD, Morrison JH (1987) Laminar and regional distributions of neurofibrillary tangles and neuritic plaques in Alzheimer's disease: a quantitative study of visual and auditory cortices. J Neurosci 7:1799–1808. https://doi.org/10.1523/JNEUROSCI.07-06-01799.1987
27. McKee AC, Cairns NJ, Dickson DW, Folkerth RD, Keene CD, Litvan I et al (2016) The first NINDS/NIBIB consensus meeting to define neuropathological criteria for the diagnosis of chronic traumatic encephalopathy. Acta Neuropathol 131:75–86. https://doi.org/10.1007/s00401-015-1515-z
28. McKee AC, Stern RA, Nowinski CJ, Stein TD, Alvarez VE, Daneshvar DH et al (2013) The spectrum of disease in chronic traumatic encephalopathy. Brain 136:43–64. https://doi.org/10.1093/brain/aws307
29. Merlini M, Wanner D, Nitsch RM (2016) Tau pathology-dependent remodelling of cerebral arteries precedes Alzheimer's disease-related microvascular cerebral amyloid angiopathy. Acta Neuropathol 131:737–752. https://doi.org/10.1007/s00401-016-1560-2
30. Oshima K, Uchikado H, Dickson DW (2008) Perivascular neuritic dystrophy associated with cerebral amyloid angiopathy in Alzheimer's disease. Int J Clin Exp Pathol 1:403–408
31. Park L, Hochrainer K, Hattori Y, Ahn SJ, Anfray A, Wang G et al (2020) Tau induces PSD95-neuronal NOS uncoupling and neurovascular dysfunction independent of neurodegeneration. Nat Neurosci 23:1079–1089. https://doi.org/10.1038/s41593-020-0686-7
32. Pooler AM, Phillips EC, Lau DH, Noble W, Hanger DP (2013) Physiological release of endogenous tau is stimulated by neuronal activity. EMBO Rep 14:389–394. https://doi.org/10.1038/embor.2013.15
33. Richard E, Carrano A, Hoozemans JJ, van Horssen J, van Haastert ES, Eurelings LS et al (2010) Characteristics of dyshoric capillary cerebral amyloid angiopathy. J Neuropathol Exp Neurol 69:1158–1167. https://doi.org/10.1097/NEN.0b013e3181fab558
34. Schindelin J, Arganda-Carreras I, Frise E, Kaynig V, Longair M, Pietzsch T et al (2012) Fiji: an open-source platform for biological-image analysis. Nat Methods 9:676–682. https://doi.org/10.1038/nmeth.2019
35. Snellman A, Lantero-Rodriguez J, Emersic A, Vrillon A, Karikari TK, Ashton NJ et al (2022) N-terminal and mid-region tau fragments as fluid biomarkers in neurological diseases. Brain 145:2834–2848. https://doi.org/10.1093/brain/awab481
36. Tarasoff-Conway JM, Carare RO, Osorio RS, Glodzik L, Butler T, Fieremans E et al (2015) Clearance systems in the brain-implications for Alzheimer disease. Nat Rev Neurol 11:457–470. https://doi.org/10.1038/nrneurol.2015.119
37. Thal DR, Ghebremedhin E, Rub U, Yamaguchi H, Del Tredici K, Braak H (2002) Two types of sporadic cerebral amyloid angiopathy. J Neuropathol Exp Neurol 61:282–293. https://doi.org/10.1093/jnen/61.3.282
38. van Veluw SJ, Hou SS, Calvo-Rodriguez M, Arbel-Ornath M, Snyder AC, Frosch MP et al (2020) Vasomotion as a driving force for paravascular clearance in the awake mouse brain. Neuron 105(549–561):e545. https://doi.org/10.1016/j.neuron.2019.10.033
39. Vidal R, Calero M, Piccardo P, Farlow MR, Unverzagt FW, Mendez E et al (2000) Senile dementia associated with amyloid beta protein angiopathy and tau perivascular pathology but not neuritic plaques in patients homozygous for the APOE-epsilon4 allele. Acta Neuropathol 100:1–12. https://doi.org/10.1007/s004010051186
40. Vilor-Tejedor N, Ciampa I, Operto G, Falcon C, Suarez-Calvet M et al (2021) Perivascular spaces are associated with tau pathophysiology and synaptic dysfunction in early Alzheimer's continuum. Alzheimers Res Ther 13:135. https://doi.org/10.1186/s13195-021-00878-5
41. Vinters HV (1987) Cerebral amyloid angiopathy. A critical review Stroke 18:311–324. https://doi.org/10.1161/01.str.18.2.311
42. Vonsattel JP, Myers RH, Hedley-Whyte ET, Ropper AH, Bird ED, Richardson EP Jr (1991) Cerebral amyloid angiopathy without and with cerebral hemorrhages: a comparative histological study. Ann Neurol 30:637–649. https://doi.org/10.1002/ana.410300503
43. Wang X, Liu Q, Li XG, Zhou QZ, Wu DQ, Li SH et al (2021) T217-phosphorylation exacerbates tau pathologies and tau-induced cognitive impairment. J Alzheimers Dis 81:1403–1418. https://doi.org/10.3233/JAD-210297
44. Yamada K, Holth JK, Liao F, Stewart FR, Mahan TE, Jiang H et al (2014) Neuronal activity regulates extracellular tau in vivo. J Exp Med 211:387–393. https://doi.org/10.1084/jem.20131685
45. Zwang TJ, Bennett RE, Lysandrou M, Woost B, Zhang A, Lieber CM et al (2023) Tissue libraries enable rapid determination of conditions that preserve antibody labeling in cleared mouse and human tissue. Elife. https://doi.org/10.7554/eLife.84112
46. Zwang TJ, Woost B, Bailey J, Hoglund Z, Richardson DS, Bennett RE et al (2023) Spatial characterization of tangle-bearing neurons and ghost tangles in the human inferior temporal gyrus with three-dimensional imaging. Brain Commun. https://doi.org/10.1093/braincomms/fcad130